RSC Advances

PAPER

View Article Online
View Journal | View Issue

Cite this: *RSC Adv.*, 2026, **16**, 16167

One-pot-synthesized anthracene-based chemodosimeter for toxic cyanide (CN^-) detection and anticancer analysis: substantiated by DFT, real-time investigations, and cytotoxicity assays

Muthaiah Shellaiah,[a] Wen-Tai Li,[*bc] Phamdom Romabai Chanu,[d] Richard Lam,[b] Arumugam Murugan,[e] Basheer Aazaad,[f] Ming-Chang Lin,[gh] K. Anandan[i] and Mayank Bhushan[j]

To preserve the ecosystem, researchers have recommended screening for CN^- ions. For the detection of CN^- ions, chemodosimetric probes play a defined role by affording diverse reaction-based responses. Here, (*E*/*Z*)-9-(2-nitrovinyl)anthracene (AN) was synthesized *via* a one-pot reaction between anthracene-9-carboxaldehyde and nitromethane. AN possesses anticancer activity and was employed as a chemodosimeter to detect CN^- ions. In the presence of CN^-, the "turn-on" photoluminescence (PL) emission enhancement at 420 nm was observed due to the formation of the 1,4-addition product 'ANCN'. The maximum PL emission for 'ANCN' was achieved within one minute and was active across the pH range of 3–11. The AN-CN^- detection system demonstrated linearity in the range of 0.01 to 500 μM, with a limit of detection (LOD) of 99.4 nM. The Job plot, based on the ultraviolet-visible (UV-vis) spectral investigation, revealed the 1 : 1 stoichiometric association between AN and CN^-, with an association constant (K_a) of 2.81×10^9 M^{-1}. Multiple spectroscopic and density functional theory (DFT) studies confirmed the formation of 'ANCN'. The energy gap variations of AN and ANCN were derived from DFT data. The analysis of strips, cotton swabs, fish pieces, real water, and herbal extracts confirmed the analytical performance of AN. The recovery of CN^- ions in real water and herbal extract was between 84.36% and 101.61%, with <5% relative standard deviation (RSD). Cytotoxicity assays in cancerous (A549 and MCF-7) and non-cancerous (WI-38 and MCF-10) cell lines defined the anticancer efficacy of AN. These findings pave the way for similar designs in the future.

Received 2nd January 2026
Accepted 23rd February 2026

DOI: 10.1039/d6ra00024j

rsc.li/rsc-advances

1 Introduction

Global population growth and increasing consumer demands drive industrial development, which produces many toxic by-products during mass manufacturing that harm the environment and living beings.[1–3] Various industries, such as chemical, bio-/electro-chemical, mining, pharmaceutical, metallic alloy, semiconductor, textile, dye, and pigment industries, generate significant amounts of toxic by-products during thmanufacturing.[4–10] The introduction of the soluble forms of toxic heavy metal ions and anions into water environments often proves fatal for living species.[11–13] Among the toxic anions, cyanide (CN^-) ions pose a severe threat to society because of their direct effect on cellular respiration, which can be fatal.[14,15] CN^- ions may enter the environment through mining, textile, electroplating, chemical, and pigment industrial wastes or their by-products.[16–20] Cyanide exposure may severely impact the respiratory system.

The reversible binding of CN^- ions disrupts the ferric (Fe^{3+}) state of cytochrome c, blocking the oxygen (O_2) supply to the respiratory system and leading to severe, fatal incidents.[21] Notably, CN^- exposure may cause immediate symptoms like headache, vomiting, shortness of breath, and confusion, followed by coma.[22,23] Given the lethal and immediate toxic impact of CN^- ions, based on research validation from multiple

[a]*Department of Chemistry, Dayananda Sagar College of Engineering, Bangalore, Karnataka, 560111, India*
[b]*National Research Institute of Chinese Medicine, Ministry of Health and Welfare, Taipei 11221, Taiwan, Republic of China. E-mail: wtli@nricm.edu.tw*
[c]*Department of Chemistry, Tamkang University, New Taipei City 251301, Taiwan, Republic of China*
[d]*College of Pharmacy, Taipei Medical University, 11031, Taiwan, Republic of China*
[e]*Department of Chemistry, North Eastern Regional Institute of Science & Technology, Nirjuli, Itanagar 791109, India*
[f]*Department of Physics, Saveetha Engineering College, Thandalam, Chennai–602105, Tamil Nadu, India*
[g]*Department of Applied Chemistry, National Yang Ming Chiao Tung University, Hsinchu 300, Taiwan*
[h]*Center for Emergent Functional Matter Science, National Yang Ming Chiao Tung University, Hsinchu 300, Taiwan*
[i]*Department of Physics, AMET University, Chennai 603 112, Tamil Nadu, India*
[j]*Department of Biotechnology, Graphic Era (Deemed to be University), Dehradun 248002, Uttarakhand, India*

studies, the World Health Organization (WHO) set its allowed limit to 1.9 μM (μM = micromole; 10^{-6} M) in drinking water.[24,25] The screening of CN^- ions is important due to their increasing presence in the environment. To date, CN^- ions have been detected and quantified using numerous nanomaterials/nanocomposites, small organic probes, metal–organic frameworks (MOFs), and conjugated dye molecules.[26–30] Additionally, methods and tactics, such as fluorometry, colorimetry, chromatography, electrochemistry, and chemiluminescence, have been developed to quantify CN^- ions.[31–35] While considering organic probe-based colorimetric and fluorometric sensing of CN^- ions, reaction-based chemodosimetric probes appear to be impressive in terms of their diverse, irreversible, and stable responses, allowing for long-term tracking.[36–38]

α,β-Unsaturated compounds with the β-position bearing an electron-withdrawing group, such as –carbonyl (–CO), nitrile (–CN), and nitro ($-NO_2$) functional units, may undergo 1,4-addition with CN^- ions, leading to diverse adduct formation, affording distinct sensor responses. Recently, our group reported the colorimetric CN^- ion-sensing ability of commercial β-nitrostyrene analogues and a demonstration using test strips.[41] β-Nitrostyrene-type organic probes with diverse fluorophores have subsequently attracted substantial research attention, and among the fluorophores, anthracene is considered effective due to its opto-electronic properties.[42–44] Many anthracene-based chemodosimeter probes have been designed for the detection of CN^- ions.[45–48] However, to date, the use of (*E*/*Z*)-9-(2-nitrovinyl)anthracene (AN) for CN^- ion quantification has not been reported, which has motivated us to proceed further with our research. Developing small organic sensory probes *via* a one-pot reaction remains an impressive and challenging task, as noted by many researchers.[49–51]

Developing organic moieties with anticancer activity requires careful optimisation of the functional groups introduced. Nitro ($-NO_2$) group-containing drugs, such as flutamide, nilutamide, nitracrine, azathioprine, and rubitecan, have already been demonstrated as effective anticancer drugs[52,53] in which the nitro ($-NO_2$) groups play a vital role in the anticancer effect.[54] Numerous organic moieties have been developed *via* multi-step synthesis,[55–57] and one-pot-synthesized molecules are attracting substantial research interest in terms of their cost-effectiveness.[58] Herein, we report the anticancer efficacy of one-pot-synthesized AN. A one-pot reaction between anthracene-9-carboxaldehyde and nitromethane afforded AN, which exhibits high selectivity for CN^- ions and shows potential anticancer activity, thus justifying its potential for application as a cost-effective probe for environmental maintenance and bio-applications.

In this work, (*E*/*Z*)-9-(2-nitrovinyl)anthracene (AN) has been synthesized from a one-pot reaction between anthracene-9-carboxaldehyde and nitromethane in the presence of acetic acid and ammonium acetate, and reported as a chemodosimetric sensor for CN^- ions in dimethyl sulfoxide (DMSO). The CN^- ions induced a photoluminescence (PL) "turn-on" response at 420 nm due to the formation of the 1,4-addition product 'ANCN'. The PL maxima of 'ANCN' were attained within one minute and were active across the 3–11 pH range. Individual ultraviolet-visible (UV-vis) and PL titrations revealed a linear response range of AN toward CN^- ions, the stoichiometry, and association constant values. Nuclear magnetic resonance (NMR), Fourier transform infrared (FTIR) spectroscopy, density functional theory (DFT), and high-resolution mass spectrometry (HR-MS) analyses have elucidated the underlying mechanism and changes in energy gaps. Studies using test strips, cotton swabs, and fish tissues have demonstrated the analytical utility of AN for CN^- ions. Significant recovery in real water samples and herbal extract analysis have authenticated the analytical application. Additionally, cytotoxic assays in cancerous (A549 and MCF-7) and non-cancerous (MCF-10 and WI-38) cell lines revealed the improved anticancer efficacy of AN, highlighting its potential in future drug modifications.

2 Experimental

Instrumental information, stock solutions, procedures for pH investigations, relative quantum yield calculations, NMR titration, HR-mass spectrometry, and FTIR spectroscopy procedures are provided in the SI.

2.1. Synthesis of AN[59,60]

In a reaction vessel, 1 g (1 equivalent) of anthracene-9-carboxaldehyde was stirred in 50 mL of glacial acetic acid under an inert atmosphere for 30 minutes. To the above vessel, 3.74 g (10 equivalents) of ammonium acetate was added, followed by the injection of 890 mg (780 μL; 3 equivalents), and the reaction was maintained under an inert atmosphere. The mixture was refluxed at 110 °C for 24 hours. The generation of the condensation adduct (*E*/*Z*)-9-(2-nitrovinyl)anthracene (AN) was confirmed by thin-layer chromatography (TLC). The crude AN was cooled to room temperature, precipitated by adding water, filtered, and dried at 50 °C for 12 hours in a hot air oven. The crude product was recrystallized three times in absolute ethanol to afford ultrapure, dark-red solids of AN. Yield: 0.883 g (73%). ^{1}H NMR (600 MHz, DMSO-d_6) δ/ppm: 8.96 (dd, J = 13.8, 0.9 Hz, 1H), 8.74 (s, 1H), 8.24 (dq, J = 8.7, 1.0 Hz, 2H), 8.17–8.11 (m, 2H), 7.91 (d, J = 13.7 Hz, 1H), 7.59 (dddd, J = 22.3, 7.8, 6.5, 1.3 Hz, 4H); ^{13}C NMR (151 MHz, DMSO-d_6) δ 144.14, 135.67, 131.16, 130.23, 129.73, 129.72, 129.38, 127.82, 126.25, 125.32, 124.31, 123.92, 40.39, 40.25, 40.11, 39.97, 39.83, 39.69, 39.55; HR-mass: calculated for $C_{16}H_{12}O_2N$ (M + 1): m/z = 250.0863; found (M + 1): m/z = 250.0868.

2.2. Solvent selection for sensor studies[61]

From a 1 mM (mM = millimole; 10^{-3} M) stock of AN, 50 μL was taken into a separate vial and diluted with 945 μL of DMSO. This solution was then shaken with 5 μL of anions from a 100 mM stock solution, adjusted to 1 mL as the final volume. The mixture was then subjected to UV-vis and PL spectroscopic analysis. The sensor responses obtained in UV-vis and PL studies were recorded and further evaluated in other solvents, such as dimethylformamide (DMF), tetrahydrofuran (THF), acetonitrile (ACN), ethanol (EtOH), and deionised (DI) water. The relative photoluminescence quantum yields (PLQYs; Φ_F) of

AN in the presence of CN^- ions were then determined, and it indicated that DMSO is an effective solvent for all sensor tests. Moreover, due to its low toxicity, DMSO has been recommended as an ideal solvent for such applications.[57] Therefore, for a single analyte test, 50 μL of AN (from a 1 mM stock) was diluted with 945 μL of DMSO, followed by 5 μL of anions (from a 100 mM stock). On the other hand, during dual analyte studies, 50 μL of AN (from a 1 mM stock) was diluted with 940 μL of DMSO, followed by 5 μL of CN^- ions (from a 100 mM stock) and μL of anions (from a 100 mM stock).

2.3. DFT calculations

DFT calculations were performed using the Gaussian16 program package, which revealed the frontier molecular orbital levels (FMOs) of AN and ANCN in both gas and DMSO media.[62] The time-dependent DFT (TD-DFT) calculations were carried out with the first 10 excitation states ($N = 10$) to obtain the simulated absorption spectra. For all electronic calculations, B3LYP (Becke-3-parameter-Lee–Yang–Parr; a hybrid GGA functional) and 6-31+G(d,p) basis sets were employed for carbon (C), hydrogen (H), nitrogen (N), and oxygen (O) atoms.[63] From FMO optimisation, the energies of the highest and lowest occupied molecular orbitals (HOMOs and LUMOs) and energy gaps (E_gs) of AN and ANCN were determined and tabulated.

2.4. Procedures for preparation of strips and cotton swabs and analysis of fish pieces[41,64]

Filter papers were cut into spherical-shaped pieces and incubated in the 100 μM AN solution for 30 minutes. These test strips were dried using a heat gun and then stored in an air oven at 50 °C for three hours. Thereafter, strips were incubated with a diverse set of anions (at 0.5 mM) in separate vials for one hour. The strips were dried under a heat gun and then placed in an air oven at 50 °C for two hours. They were subsequently subjected to photography under a UV lamp ($\lambda_{ex} = 365$ nm). A similar procedure was followed for the strips of AN with increasing concentration of CN^- ions (100, 200, 300, 400, and 500 μM; $n = 5$).

In the 100 μM AN solution, the cotton buds were incubated for one hour, dried under a heat gun for 3–5 minutes, and then kept in an air oven for one day. The buds were then dipped into various anion solutions (at 0.5 mM) in separate vials for one hour. The buds were dried under a heat gun for 3–5 minutes and kept in an air oven for one day. Under the UV lamp ($\lambda_{ex} = 365$ nm), the buds were photographed to define the solid-state sensing ability of AN. A similar procedure was followed with varied concentrations of CN^- ions (100, 200, 300, 400, and 500 μM; $n = 5$).

Fish were purchased from the Beitou market located in Taipei, Taiwan (ROC) and were cut into small pieces. The fish pieces were washed with DI water and dried in the air oven for four hours. After incubating these pieces in a 200 μM AN solution for one day, they were dried using a heat gun for 5–10 minutes and then stored in an oven at 50 °C for one day. The pieces were then dipped into various anions (at 0.5 mM) in separate vials for six hours. The pieces were removed and dried under a heat gun for 5–10 minutes, then placed inside an oven at 50 °C for one day. Photography under a UV lamp revealed the sensing ability of AN toward CN^- ions in fish pieces. A similar procedure was employed for incremental concentrations of CN^- ions (100, 200, 300, 400, and 500 μM; $n = 5$).

2.5. Procedure for real and herbal water recovery[65,66]

Soil-water, Radix Hedysari, and Nelumbinis Stamen extracts were prepared according to the earlier literature.[64] The CN^- ions were prepared at 10 mM concentrations in tap water, soil-water extract, Radix Hedysari extract, and Nelumbinis Stamen extract. To the mixture of 50 μL AN (from 1 mM stock in DMSO) and 900 μL of DMSO, the varied concentrations of CN^- ions (50 μM, 100 μM, and 300 μM (for tap water); 25 μM, 100 μM, and 200 μM (for soil water); 50 μM, 150 μM, and 200 μM (for Radix Hedysari extract); 75 μM, 100 μM, and 150 μM (for Nelumbinis Stamen extract)) from 10 mM stock were spiked and diluted with DMSO to achieve a 1 mL final volume. The samples were thoroughly shaken, and the PL recovery for each concentration was documented as proof. The above procedure was repeated three consecutive times to tabulate the standard deviation (SD) and relative standard deviation (RSD) values.

2.6. Cytotoxicity/SRB assay procedure

The SRB assay defines the anti-proliferative effects of AN.[67] Cancerous (A549 and MCF-7) and non-cancerous (WI-38 and MCF-10) cell lines were mainly obtained from the Bioresource Collection and Research Center (BCRC), Food Industry Research and Development Institute (FIRDI), Taiwan. For overnight cultivation, the cancerous (A549 and MCF-7) and non-cancerous (WI-38 and MCF-10) cell lines were grown in 96-well plates. To establish a baseline (T_0), four wells with 10% trichloroacetic acid (TCA) were used for AN incubation. AN, at 1.25, 2.5, 5, 10, and 20 μM, was incubated for 24 hours. Thereafter, the addition of 10% TCA terminated cell growth, which was then rinsed with phosphate-buffered saline (PBS) and dried in air. Next, 0.4% sulforhodamine B (SRB) in 1% acetic acid was used to stain the cell lines, which were incubated for 10 minutes at room temperature. The addition of 1% acetic acid removed the excess dye, and then the sample was dried in air. The 10 mM Tris–base solution dissolves the attached SRB, which the Epoch 2 microplate reader measured at 515 nm.

By comparing the absorption values of the baseline (T_0), control (C), and treated samples (T_x), cell proliferation was assessed and the percentile growth inhibition was attained using the formula as follows:

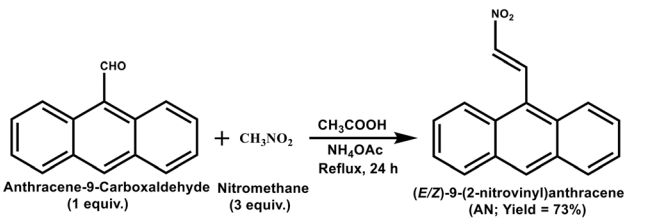

Scheme 1 Synthesis of AN: anthracene-9-carboxaldehyde (1 equiv.) and nitromethane (3 equiv.) were refluxed for 24 hours to afford '(E/Z)-9-(2-nitrovinyl)anthracene (AN)' with 73% yield.

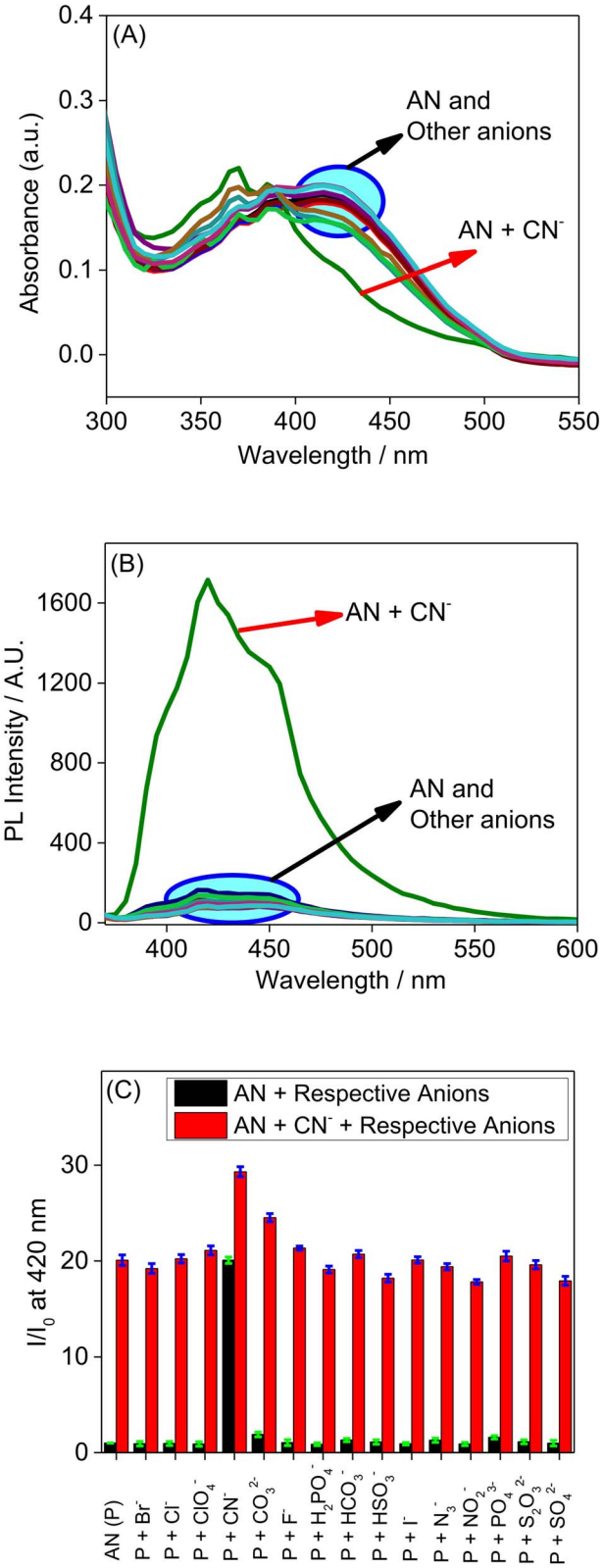

Fig. 1 (A) UV-vis selectivity of AN (50 μM in DMSO; λ_{ex} = 345 nm and λ_{em} = 420 nm) for 500 μM of anions. (B) PL selectivity of AN (50 μM in DMSO; λ_{ex} = 345 nm and λ_{em} = 420 nm) for 500 μM anions. (C) Bar graph representing the single- and dual-analyte selectivity of AN (50 μM in DMSO; λ_{ex} = 345 nm and λ_{em} = 420 nm) for CN^- ions (for single analyte studies, 50 μM of AN in DMSO was mixed with 5 μL of anions (from 100 mM stock; n = 5) and for dual analyte studies, 50 μM of AN in DMSO was mixed with 5 μL of CN^- ions (from 100 mM stock) and with 5 μL of anions (from 100 mM stock; n = 5).

$$100 - [(T_x - T_0)/(C - T_0)] \times 100 \text{ (when } T_x > T_0) \text{ or}$$

$$100 - (T_x - T_0) \times 100 \text{ (when } T_x < T_0).$$

3 Results and discussion

3.1. Synthesis and photophysical properties

The AN chemodosimeter was synthesized *via* refluxing the anthracene-9-carboxaldehyde and nitromethane in the presence of acetic acid and ammonium acetate for 24 hours, as shown in Scheme 1.[59,60] The purity of AN was confirmed by ^{1}H, ^{13}C, and HR-MS data, as depicted in Fig. S1–S3 (SI). The absorbance of AN (50 μM in DMSO) was observed at 225 nm, 240 nm, and 420 nm, with a weak PL emissive band at 420 nm upon excitation at 345 nm. The Φ_F value of AN was determined to be 0.92% relative to the reference standard 9,10-diphenylanthracene (Φ_F = 70% in DMSO).

3.2. Solvent selection for sensor studies

Before detailing the sensory investigations, a suitable solvent system was justified as follows. As explored in subsequent sections, the AN probe (50 μM in DMSO) shows a PL "turn-on" response in the presence of CN^- ions (500 μM) compared with other anions (500 μM). For AN + CN^-, the enhancement (I/I_0) and percentile Φ_F values were established to be 20.08% and 18.73%, respectively. The I/I_0 values of AN + CN^- in DMF, EtOH, ACN, THF, and DI-water were found to be 18.76, 7.11, 12.42, 10.05, and 4.78, respectively. Likewise, the percentile Φ_F values of AN + CN^- in DMF, EtOH, ACN, THF, and DI-water are appraised to be 17.34%, 6.65%, 11.56%, 9.54%, and 3.78%, respectively. Table S1 summarizes the I/I_0 and Φ_F values of AN + CN^- in various solvents. The sensor response of AN to CN^- ions was found to be higher in DMSO than in other solvents. Moreover, DMSO has been reported to be a low-toxicity, biocompatible solvent, suitable for biological studies.[68] Thus, DMSO was selected for all subsequent sensory interrogations.

3.3. Sensor selectivity of AN for anions

To investigate the selectivity of AN, 500 μM of anions such as Cl^- (chloride), Br^- (bromide), I^- (iodide), CN^- (cyanide), F^- (fluoride), ClO_4^- (perchlorate), SO_4^{2-} (sulfate), $S_2O_3^{2-}$ (thiosulfate), PO_4^{3-} (phosphate), HCO_3^- (bicarbonate), NO_2^- (nitrite), $H_2PO_4^-$ (dihydrogen phosphate), CO_3^{2-} (carbonate), HSO_3^- (bisulfite), N_3^- (azide), CA (cysteamine), Cys (cysteine), Na_2S (sodium sulfide), and GSH (glutathione) were added to 50 μM of AN in DMSO and subjected to UV/PL spectral studies. In the presence of CN^- ions, the absorbance at 420 nm blue-shifted to 412 nm with a decrease in intensity, as shown in A and S4 (ESI). At the same time, the remaining anions did not affect the absorbance spectra. Similarly, a strong "turn-on" PL

emission was observed for CN^- ions at 420 nm (λ_{ex} = 345 nm), as shown in B. None of the other anions showed similar PL enhancement.

To confirm the high selectivity of AN for CN^- ions, the interference effect was investigated. Similar to single-analyte studies, the PL response of AN + CN^- was not affected by the presence of other anions, as illustrated in Fig. 1C. Notably, >17-fold PL enhancement was observed in the presence of all anions. Thus, the greater sensor selectivity of AN for CN^- was undoubtedly validated. This irreversible sensor response also suggests a feasible reaction-based mechanism. The colorimetric photograph of AN with anions is shown in Fig. S5 (SI), in which a moderate color deficiency is pictured for CN^- ions compared with other anions. Fig. 2 illustrates the PL "turn-on" response of AN for CN^- ions compared with other anions.

The weakly emissive AN is not significantly affected in the presence of other anions. However, it exhibits a strong blue emission in the presence of CN^- ions under UV lamp irradiation at 365 nm. These results authenticate the high sensor selectivity of AN for CN^- ions. Similar to the experimental absorbance, the TD-DFT-optimized absorbance explores the feasible fluorescence resonance electron transport (FRET) mechanism discussed in Section 3.8.

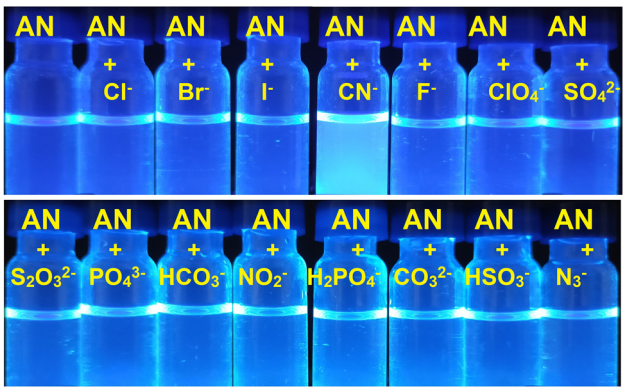

Fig. 2 Photographs showing the fluorometric selectivity of AN (50 μM in DMSO) towards 500 μM of anions under UV-lamp irradiation (λ_{ex} = 365 nm).

3.4. Effects of pH and time on the CN^- sensor

To identify the optimal operating pH for CN^- ion detection, the effect of pH on AN and AN + CN^- was investigated. A negligible effect was observed between pH 3 and 11 for both AN and AN + CN^-, as shown in Fig. 3A. However, at higher hydroxyl (-OH) concentrations, the 1,4-addition-facilitated CN^- sensing is strongly affected by disturbances to the protonation step. At pH 1 and 2, HCN formation is induced, which prevents ANCN generation, and high basic pH values affect the probe itself. Thus, pH 3–11 was suggested as a suitable operating pH condition. Similarly, the sensor response of AN to CN^- ions reaches its maximum fluorescence intensity within 60 seconds (1 minute), as shown in Fig. 3B. Thereafter, the PL intensity of AN + CN^- becomes saturated, indicating a rapid reaction that leads to fluorescence emission. The effect of time on CN^- ion detection also supports the notion that the proposed chemodosimetric 1,4-addition reaction is rapid and can be effective for real-time investigations.

3.5. Linear range and detection limit

The sensing efficacy of AN toward CN^- ions has been validated by its linear range of detection and LOD. To define the linear regression, individual PL titrations of AN (50 μM in DMSO) were performed with varying concentrations of CN^- ions (0–500 μM). During the titration, the PL emission of AN at 420 nm was enhanced, as shown in Fig. 4A.

On plotting the [CN^-] *vs.* PL fold of enhancement at 420 nm (I/I_0; see Fig. 4B), the linear range of CN^- sensing was observed in the range of 0.01–500 μM ($Y = 0.03801x + 0.9963$; $R^2 = 0.99856$; $n = 5$) with a calculated limit of detection (LOD) of 99.4 nM (nM = 10^{-9} M; LOD = 3σ/slope; where σ was obtained from 10 consecutive measurements of the probe's PL intensity at 420 nm). The appraised linear range and nanomolar LOD of AN for CN^- ions clarify the effectiveness of the designed chemodosimetric probe, which allows us to move toward unique applications. Next, similar to the changes in PL, the UV-vis

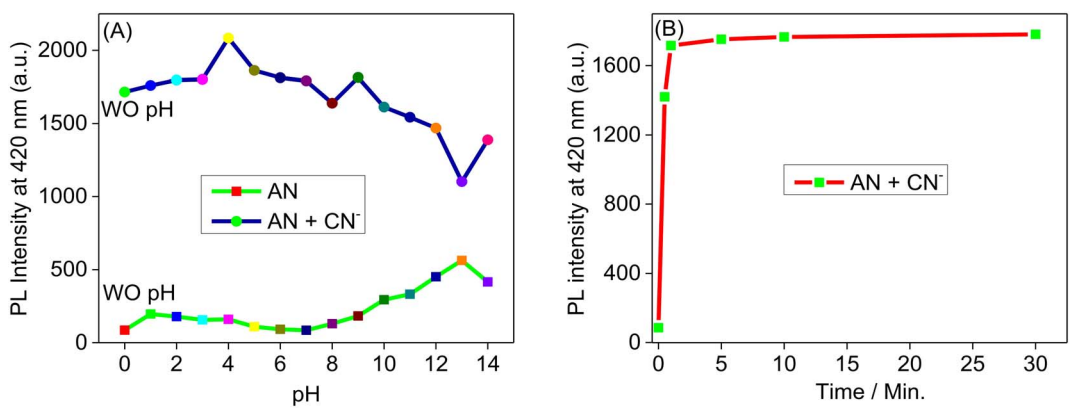

Fig. 3 (A) Effects of pH on AN and AN + CN^-, monitored by the PL intensity at 420 nm. (B) Effect of time on the response of the AN sensor to CN^- ions monitored by the PL intensity at 420 nm.

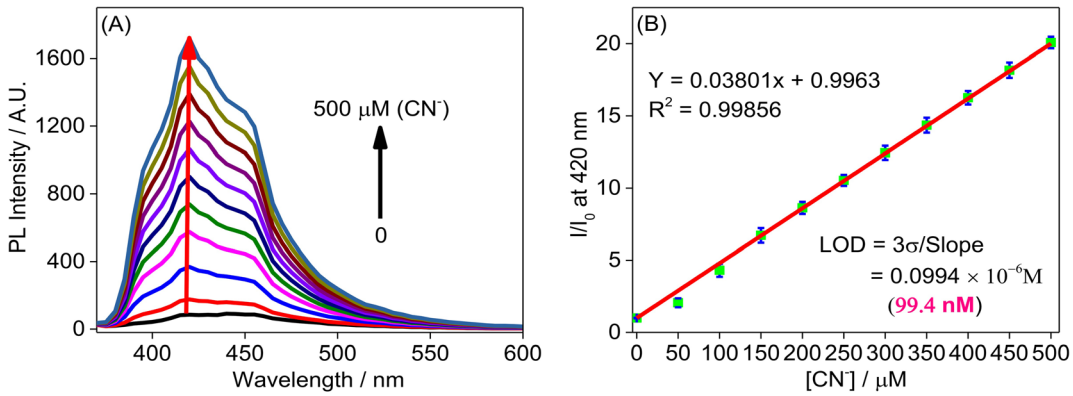

Fig. 4 (A) PL titration of AN (50 μM in DMSO) with CN^- ions (tetra-*n*-butylammonium cyanide (TBACN); 0–500 μM with an equal span of 50 μM). (B) Linear regression plot of AN to CN^- ions monitored by the PL intensity at 420 nm for limit of detection (LOD) calculation ($n = 5$).

titration of AN with 0–500 μM of CN^- ions also revealed changes, as shown in Fig. S6A and B SI. The absorbance at 420 nm was quenched and blue-shifted to 412 nm until a specific concentration was reached, after which it partially reverted, allowing us to calculate the stoichiometry as described in further detail.

3.6. Stoichiometry and association constant

The stoichiometric association of CN^- ions with AN was established from the UV-vis titration (see Fig. S6B SI). As shown in Fig. 5A, the Job plot of the mole fraction of CN^- ions ($X_M = [AN]/[AN] + [CN^-]$) *vs.* $1/A_{420\ nm}$ showed a maximum at a mole fraction of *ca.* 0.501, suggesting a 1 : 1 stoichiometric association in the 1,4-addition. However, a higher CN^- ion concentration was used to achieve the stable chemodosimetric product ANCN. Consistent with the 1 : 1 stoichiometry, the Benesi–Hildebrand (BH) plot between $1/[CN^-]$ *vs.* $1/I - I_0$ at 420 nm was linear, from which the association constant (K_a) was determined, as shown in Fig. 5B. From the BH-plot, the K_a value of AN to CN^- ions was appraised as $2.81 \times 10^9\ M^{-1}$. This high K_a value also indicates a highly feasible 1,4-addition reaction of AN with CN^- ions, in which the CN^- ions attack the α-unsaturated carbon (4th-position) with high affinity, followed by protonation at the β-carbon (3rd-position) to afford the desired adduct. The stoichiometry and association constant studies also support the rapid detection of CN^- ions *via* a 1,4-addition-driven chemodosimeter response.

3.7. Sensing mechanism

To establish the precise sensing mechanism, ^1H NMR titrations, HR-MS, and FTIR interrogations were carried out in sequence. Upon the addition of 0.5–3 equivalents of CN^- ions (tetra-*n*-butylammonium cyanide (TBACN); 5 mM, 10 mM, and 30 mM in DMSO-d6) to the AN (10 mM in DMSO-d6), the spectrum was affected due to the formation of the 1,4-addition adduct ANCN, as shown in Fig. S7 SI. The addition of CN^- ions at 0.5 and 1 equivalents leads to the slow disappearance of doublets at 8.96 ppm and 7.91 ppm (related to the –CH=CH– of AN), suggesting the 1,4-addition reaction. At one equivalent of CN^- ions, a triplet peak at 6.25 ppm and multiplets at 3.55 ppm and 3.70 ppm appeared, along with red and blue-shifted aromatic anthracene peaks. However, the singlets at 6.42 ppm and 7.08 ppm and the broadened multiple proton spectrum between 7.4 ppm and 7.8 ppm can be attributed to the equilibrium between AN and ANCN due to the multiple

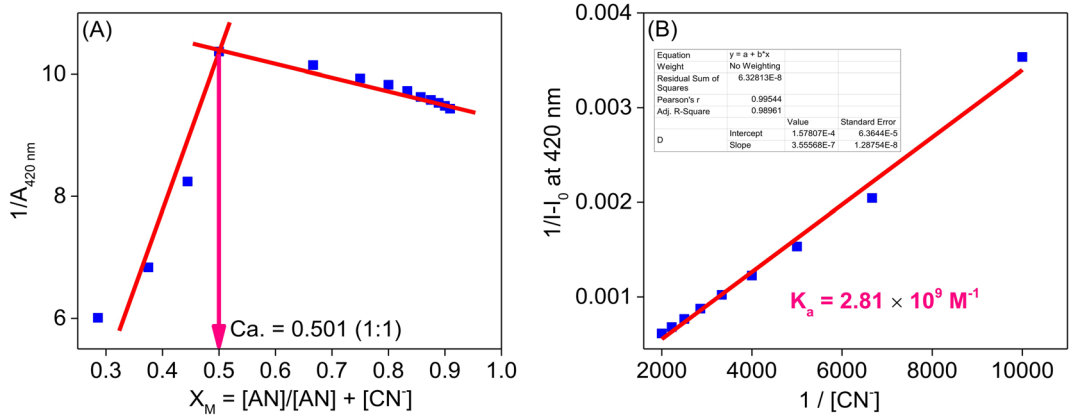

Fig. 5 (A) Job plot of the mole fraction ($X_M = [AN]/[AN] + [CN^-]$) *vs.* $1/A_{420\ nm}$, defining the 1 : 1 stoichiometry of AN to CN^- ions. (B) Benesi–Hildebrand plot of $1/[CN^-]$ *vs.* $(1/I - I_0)$ at 420 nm, estimating the association constant (K_a) between AN and CN^- ions.

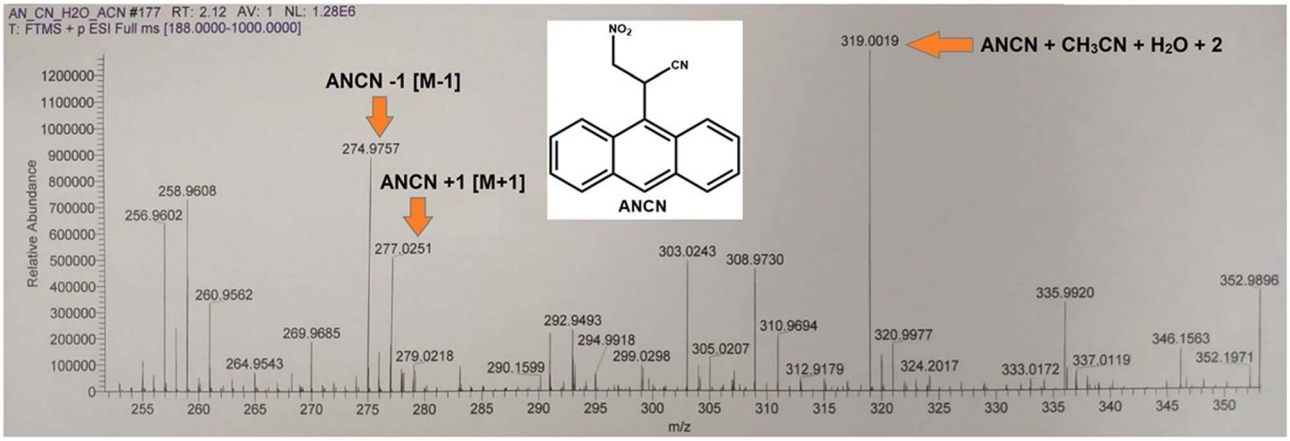

Fig. 6 Mass spectrum of AN in the presence of CN^- ions, representing the formation of the proposed ANCN compound *via* 1,4-addition (Michael addition).

intramolecular hydrogen-bonding (H-bonds) interactions of –NO_2, –CN with the H-atoms of AN and ANCN. Thus, to attain stable ANCN formation, three equivalents of CN^- ions were added and recorded. In which, a stable triplet at 6.25 ppm and multiplets at 3.54 ppm and 3.69 ppm with the disappearance of former unsaturated proton doublets and singlets at 6.42 ppm and 7.08 confirm the ANCN formation. However, due to the multiple intramolecular H-bonds driven by –NO_2, and –CN with H-atoms of ANCN, a distinct aromatic proton environment was observed between 7 ppm and 10 ppm. Additionally, the ^{13}C-NMR spectra of AN with three equivalents of CN^- ions revealed new peaks at 62.42 ppm and 79.69 ppm (see Fig. S8 SI), suggesting the ANCN formation with the nitrile group. The existence of multiple ^{13}C-NMR peaks between 115 ppm and 180 ppm also supports the H-bonds between the –NO_2 and –CN groups and the H-atoms of ANCN. Thus, based on ^{1}H and ^{13}C NMR data, the formation of ANCN was validated, which was further confirmed by HR-MS and FTIR spectroscopy.

As shown in Fig. 6, the HR-mass peak at $m/z = 274.9757$, $m/z = 277.0251$, and $m/z = 319.0019$ were assigned to ANCN-1 (M − 1), ANCN + 1 (M + 1), and ANCN + CH_3CN + H_2O + 2, respectively, supporting ANCN formation. The mass data also indicated the existence of multiple H-bonds *via* peaks at $m/z = 319.0019$, $m/z = 335.9920$, and $m/z = 352.9896$.

The FTIR spectrum of AN (see Fig. S9 SI) displays –CH stretching at 3050 cm^{-1} and –CH out-of-plane bending at 719 cm^{-1}. The aromatic stretching, –NO asymmetric, and –NO symmetric stretching vibrations are located at 1620 cm^{-1}, 1498 cm^{-1}, and 1326 cm-1, respectively. In contrast, the FTIR spectrum of AN in the presence of CN^- ions has distinct peaks, as shown in Fig. S10 (SI). The aliphatic –CH, aromatic –CH, and out-of-plane –CH bending vibrations are observed at 2863 cm^{-1}, 2958 cm^{-1}, and 729 cm^{-1}, respectively. Symmetric and asymmetric NO stretching are located at 1325 cm^{-1} and 1575 cm^{-1}, respectively. Impressively, the nitrile –CN stretching at 2152 cm^{-1} authenticates the formation of ANCN. Additionally, a broad band at 3384 cm^{-1} supports the intramolecular H-bonding of NO_2 and –CN groups and the H-atoms of ANCN. The FTIR spectrum of TBACN is shown in Fig. S11 (SI) for comparison. A low-intensity –CN peak was observed at 2102 cm^{-1}, along with –CH and –NH stretching vibration peaks. Thus, the formation of ANCN was also confirmed by FTIR spectroscopy. These FTIR variations were further validated by DFT studies, as detailed in Section 3.8.

As explored in Scheme 2, the sensing mechanism follows two steps: (i) the CN^- attacks the α (4th)-position and undergoes addition to generate a negative charge (−ve) over the β (3rd)-position. (ii) Protonation at the β-carbon leads to the formation of the nucleophilic addition product 'ANCN' with PL emission.[41]

3.8. DFT debriefings

The identification of variations in the energy gap for AN and ANCN can further validate the reaction-based chemodosimetric

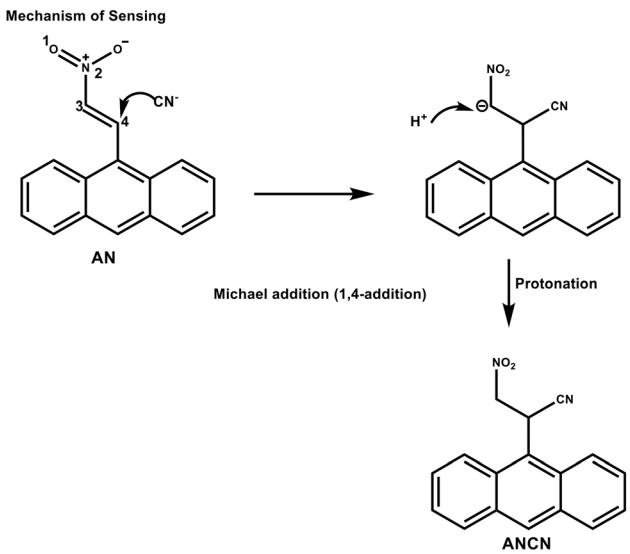

Scheme 2 Mechanism of the sensing of CN^- ions by AN. CN^- attacks the α (4th)-position and undergoes addition to generate a negative (−ve) charge over the β (3rd)-position, followed by protonation at the β-carbon which forms the ANCN, which is a nucleophilic addition compound.

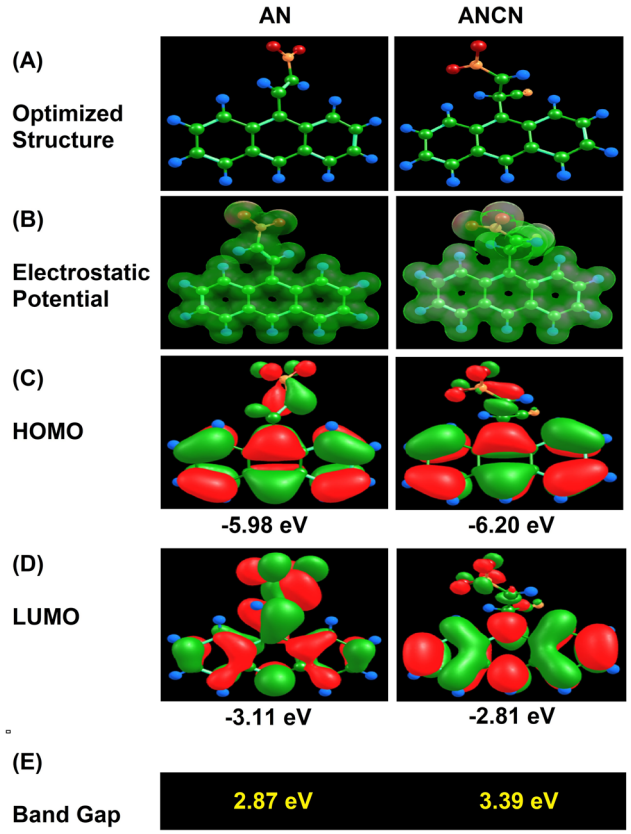

Fig. 7 (A) Optimized structures, (B) electrostatic potential, (C) HOMOs, (D) LUMOs, and (E) energy gaps of AN and ANCN using the B3LYP/6-31+G(d,p) level of theory in the gas phase.

sensory approach. Thus, DFT optimization using the B3LYP (Becke-3-parameter-Lee–Yang–Parr; a hybrid GGA functional) and 6-31+G(d,p) basis set was performed. The optimized structures of AN and ANCN in the gas phase are shown in Fig. 7A. The electrostatic potential (ESP) map of AN (see Fig. 7B) defines electronic clouds over the nitro (–NO_2) group of AN. In contrast, the electronic cloud is partially affected due to the presence of the nitrile group (–CN) in ANCN, as shown in Fig. 7B.

The HOMO, LUMO, and energy gap (E_g) values of AN have been calculated as −5.98 eV (eV = electron volts), −3.11 eV, and 2.87 eV, respectively, as depicted in Fig. 7C–E. Likewise, the HOMO, LUMO, and E_g values of ANCN have been appraised as −6.20 eV, −2.81 eV, and 3.39 eV, respectively (see Fig. 7C–E). The gas phase-optimized HOMOs (HOMO, HOMO+1, and HOMO+2) and LUMOs (LUMO, LUMO−1, and LUMO−2) are shown in Fig. S12 and S13 (SI). Similar to the gas phase-based calculation, the DMSO solvent-mediated investigation yielded consistent energy gap values of 2.56 eV and 3.32 eV for AN and ANCN, respectively. The optimized structures, ESP, HOMOs, LUMOs, and E_g values obtained using the DMSO solvent phase are shown in Fig. S14–S16 (SI). Table S2 (SI) summarizes the HOMOs, LUMOs, and E_g values of AN and ANCN in the gas phase and DMSO solvent phase. The observed energy gap variations for AN and ANCN support the reaction-based chemodosimetric approach, which led to enhanced emission. The DFT analysis shows that the FRET from anthracene to the –NO_2 group, facilitated by the –C=C– conjugation, breaks down and is partially redirected toward the –CN group of the ANCN, leading to emission enhancement. To clarify the FRET mechanism, TD-DFT optimization was carried out. For AN, the TD-DFT results show the absorbance maxima at 273 nm in the gas phase and 289 nm and 296 nm in the DMSO phase. In contrast, for ANCN, the TD-DFT-based absorbance maxima were observed at 400 nm and 416 nm in the gas and DMSO phases, respectively. These observations support the proposed FRET mechanism. Fig. S17 and Table S3 (SI) display the TD-DFT results. Next, the DFT-based FTIR spectra of AN and ANCN in the gas and DMSO phases show the relevant changes observed in the experimental results. In particular, the stretching vibrations of the aromatic region, nitro (–NO_2 (asymmetric and symmetric)), nitrile (–CN) have similar peaks between 1300–1700 cm^{-1}, as seen in Fig. S18 (SI). These observations also provide theoretical validation for ANCN formation and support the experimental results.

3.9. Analytical validation

To validate the analytical utility of AN-based CN^- ions detection, test strips, cotton swabs, fish pieces, and real samples-based recovery analysis were carried out in detail. As shown in Fig. 8A–C, the incubation of AN along with all anions revealed a stronger blue emissive strip, cotton swab, and fish piece for the CN^- ion than for other anions. Further, upon treating the AN with 0–500 μM (with an equal span of 100 μM) of CN^- ions, the slow emission enhancement was witnessed, as exposed in Fig. 8D–F. These results confirm the ability of AN to detect CN^- ions in solid-state and food samples. Thus, it has been proven

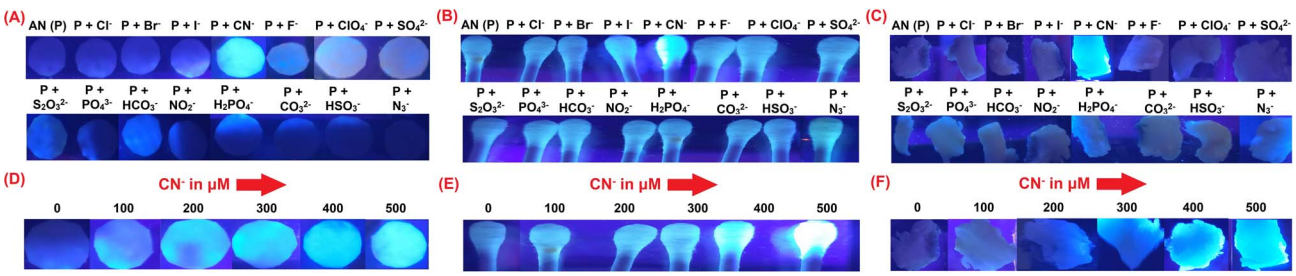

Fig. 8 (A–C) AN selectivity for anions demonstrated in test strips, buds, and fish tissues, respectively. (D–F) AN selectivity for CN^- at 0–500 μM (with an equal span of 100 μM) in test strips, cotton swabs, and fish pieces, respectively.

Table 1 Recovery data and RSD values for AN with CN^- (TBACN) in real water and herbal extract samples *via* three parallel measurements

Analyte	Real sample	Spiked (μM)	Found ± SD (μM)	Recovery (%)	RSD (%)
CN^-	Tap water	50	43.67 ± 0.05	87.44	1.08
		100	92.3 ± 0.03	92.33	3.11
		300	277.17 ± 0.07	92.41	4.32
	Soil water extract	25	21.01 ± 0.08	84.36	2.23
		100	89.26 ± 0.045	89.24	1.77
		200	194.61 ± 0.01	97.31	1.56
	Radix Hedysari extract	50	44.1 ± 0.04	88.28	2.21
		150	149.2 ± 0.18	99.52	3.83
		200	203.12 ± 0.06	101.59	2.44
	Nelumbinis Stamen extract	75	74.67 ± 0.08	99.67	4.65
		100	97.21 ± 0.03	97.24	0.92
		150	152.3 ± 0.11	101.61	1.46

that our one-pot-synthesized probe AN is a cost-effective probe for the real-time sensing of CN^- ions.

The AN-based recovery of CN^- ions in real samples was then investigated in detail. On spiking tap water, soil extract water, Radix Hedysari extract, and Nelumbinis Stamen extract with varied concentrations of CN^-, the recovery percentiles were estimated to be between 84.36% and 101.61% with <5% RSD values. Notably, the spiking of CN^- ions in tap water and soil water extract was moderately affected due to the complex matrices present in tap water and soil. In contrast, the spiking of CN^- ions in Radix Hedysari extract and Nelumbinis Stamen extract showed >88% recovery with RSD values of <5%. These observations on recovery studies also justified the cost-effective solution-based sensing ability of AN toward CN^- ions in real samples. Table 1 summarizes the recovery and RSD percentiles for CN^- ions in real samples.

3.10. Anticancer potential of AN

To assess the anticancer efficacy of AN, the SRB assay was performed in A549 and MCF-7 (lung and breast cancer) cell lines. Fig. 9A and B demonstrate that the cell viability of AN in A549

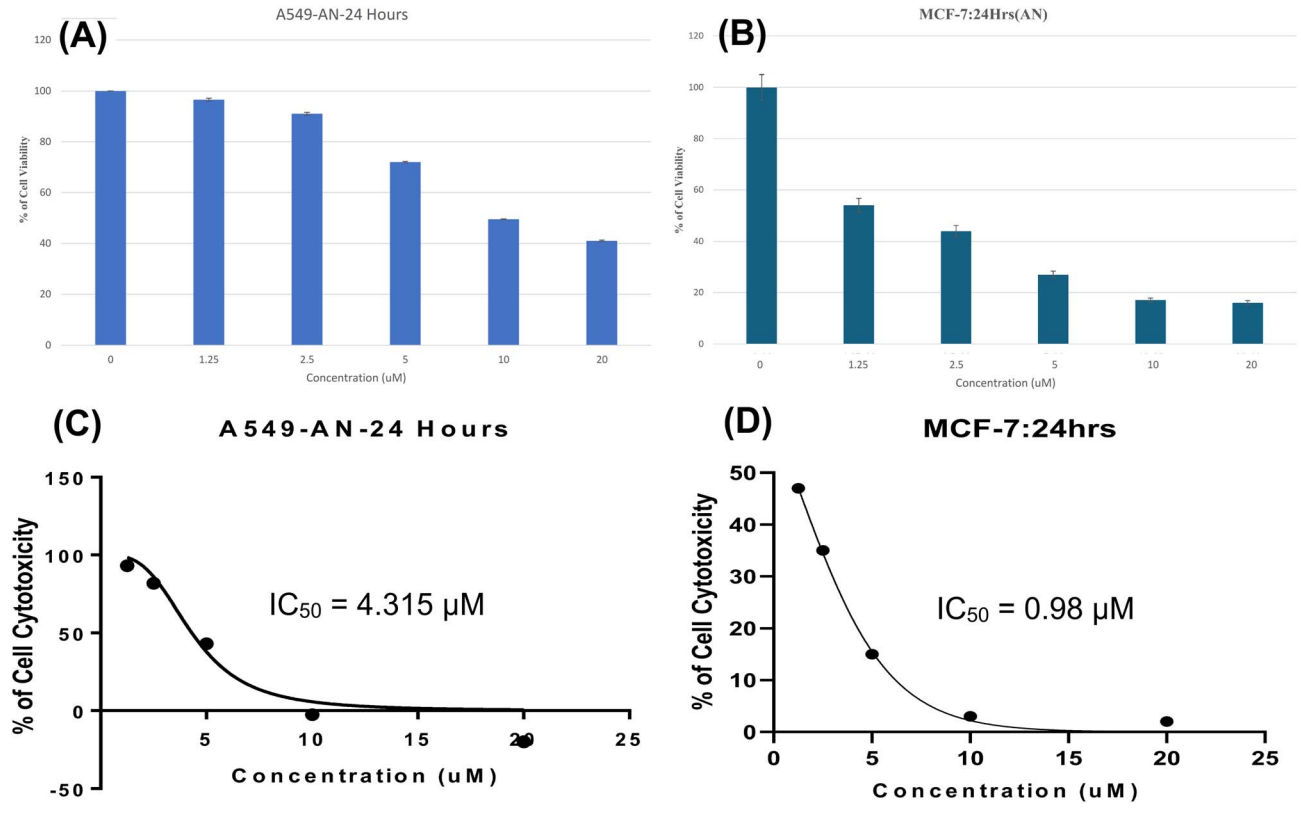

Fig. 9 (A and B) SRB assay-derived cell viability percentiles of AN in cancerous (A549 and MCF-7) cell lines ($n = 4$). (C and D) SRB assay-derived cell cytotoxicity percentiles of AN in cancerous (A549 and MCF-7) cell lines ($n = 4$) for the demonstration of its anticancer potential.

Table 2 Comparative account of AN-based CN^- ion detection relative to earlier reports[a]

Probe/system	Method of detection	Linear range	Limit of detection (LOD)	Analytical validation/additional applications	Ref.
Coumarin-based probe DHMH	Fluorescence	5.0–11.0 μM	0.64 ± 0.13 μM	Cellular imaging, cotton swabs and real water analysis/NA	23
Rosmarinic acid-capped silver nanoparticles	Colorimetry	0.01–90 μM	10 nM	Test strips and real water analysis/NA	24
Tetraphenylethylene (TPE)-CuI complex	Fluorescence	1–500 μM	100 nM	Real water analysis/NA	27
Copper-based porphyrin metal–organic frameworks (Cu-TCPP) nanosheets	Colorimetry	0.08–30 μM	57 nM and 43 nM	Real water and serum analysis/NA	28
Au–AgI NPs	Colorimetry	0–75/0.2–4 μM and 4–15 μM	150 nM and 69 nM	Real water and food sample analysis/NA	32
LCN-2	Chemiluminescence	0–100 μM	294 nM	Food sample analysis/NA	35
1,3-Indanedione-based probe	Fluorescence and colorimetry	0–20 μM	170 nM	Test strip and real water analysis/NA	36
Chromone and benzothiazole-based probe DBTC	Fluorescence	0–3 μM	5.76 nM	Test strips and cellular imaging/NA	38
Benzothiazole-based probe PDBT	Fluorescence and colorimetry	0.1–1 μM	620 nM	Real water analysis/NA	39
B-Nitrostyrene analogues P1–P4	Colorimetry	0.1–1000 μM	574 nM to 38.8 μM	Test strips and real water analysis/NA	41
(*E*/*Z*)-9-(2-Nitrovinyl)anthracene (AN)	Fluorescence	0.01–500 μM	99.4 nM	Test strips, cotton swabs, fish pieces, and real sample analysis/Anticancer activity studies	This work

[a] NA = Not Available.

and MCF-7 cell lines was affected at concentrations of 5 μM and 1.25 μM, respectively. This suggests the feasible anticancer potential of AN due to the presence of the $-NO_2$ group. Furthermore, the cytotoxicity assay confirmed the anticancer potential of AN based on IC_{50} values (the concentration required to induce 50% anticancer cell death). As shown in Fig. 9C and D, the nonlinear plot of AN concentration *versus* % cell toxicity estimated the IC_{50} values of 4.315 μM and 0.98 μM in the A549 and MCF-7 cell lines, respectively. To reassess the anticancer potential of AN, the SRB assay was conducted in non-cancerous cell lines such as WI-98 and MCF-10. Although AN showed similar results to the cancerous cells, the IC50 values were estimated to be higher. As shown in Fig. S19 (SI), the IC50 values of AN in the WI-98 and MCF-10 cell lines were 5.572 μM and 2.73 μM, respectively. These slightly higher IC_{50} values suggest that (1) AN has higher toxicity toward the cancerous cells and (2) a suitable further modification may enhance its anticancer potential, which can also act as a chemosensor material for CN^- ion detection.

These results strongly support the preliminary anticancer efficacy of AN. However, due to the high cytotoxicity of AN, we were unable to perform *in vitro* and *in vivo* bioimaging of CN^- ions. The presence of the $-NO_2$ functional group might be the primary reason for the anticancer effect, which can be extended to comparative cancer studies with existing nitro drugs. Thus, based on these preliminary data, we are currently conducting *in vitro* and *in vivo* anticancer studies in multiple cancer cell lines and mouse models.

3.11. Comparative account and advantages

The AN probe demonstrated high selectivity for CN^- ions, with a linear range of 0.01–500 μM and an LOD of 99.4 nM. As shown in Table 2, its linear range and LOD are comparable with those reported for small-molecular organic probes, chemodosimeters, nanoparticles, MOFs, and complexes that exhibit fluorescence, colorimetric, and chemiluminescence responses to CN^- ions.

The advantages of this probe are as follows: (1) this is a one-pot-synthesized probe, which avoids the use of many chemicals and is cost-effective.[40] (2) Since the probe shows high selectivity for CN^- ions and also shows anticancer potential, it can be denoted as a multifunctional probe. (3) The use of DMSO solvent for the dissolution of AN in sensory and anticancer studies avoids the solvent-tuned toxicity and is operative in real time. (4) The sensing demonstration of AN + CN^- in test strips, cotton swabs, and fish pieces demonstrated the advantage of using AN for CN^- detection in solid-state and food samples. (5) The spiked real water and herbal extract-based recovery of CN^- ions by AN demonstrated its effectiveness in environmental water analysis. (6) The cytotoxicity assays of AN in cancerous (A549 and MCF-7) and non-cancerous (MCF-10 and WI-38) cell lines indicate the anticancer potential of AN, which could be noted as an added advantage for multifunctional innovations.

4 Conclusions

The obtained results show that AN is an effective chemosensory probe for the real-time detection of CN^- ions and can be

employed in anticancer studies. The strong PL "turn-on" response of AN at 420 nm for CN^- ions among various anions demonstrated its high selectivity, which has a negligible interference effect. The probe AN showed exceptional linear regression from 0.01 to 500 μM with a LOD of 99.4 nM. The Benesi–Hildebrand plot, pH effect, and time effect show the effectiveness of AN toward CN^- ion discrimination. Notably, the ^1H NMR titration, HR-MS, and FTIR interrogations confirmed the proposed chemodosimetric product formation. The energy gap variation, appraised by DFT and TD-DFT investigations, supports the chemodosimetric adduct formation and feasible FRET-based mechanism. Impressive application in test strips, cotton swabs, fish pieces, real water, and herbal extract recoveries have demonstrated real-time detection. Additionally, the cytotoxicity SRB assays of AN in cancerous (A549 and MCF-7) and non-cancerous (MCF-10 and WI-38) cell lines illustrate its preliminary anticancer potential. These findings also support the progression of our research toward extended food toxicity screening for CN^- ions and cancer/tumour treatment.

Author contributions

Muthaiah Shellaiah: original draft–writing, conceptualization, methodology, data curation, review, and editing; Wen-Tai Li: supervision, project administration, methodology, funding acquisition, review, and editing; Phamdom Romabai Chanu: data curation, formal analysis review, and editing; Richard Lam: data curation, formal analysis review, and editing; Arumugam Murugan: data curation, formal analysis, review, and editing; Basheer Aazaad: DFT analysis, review, and editing; Ming-Chang Lin: DFT analysis, supervision, review, and editing; K. Anandan: formal analysis, review, and editing; and Mayank Bhushan: data curation, formal analysis review, and editing.

Conflicts of interest

The authors declare that they have no known competing financial interests or personal relationships that could have appeared to influence the work reported in this paper.

Data availability

The data supporting this article have been included as part of the supplementary information (SI). Supplementary information: Tables S1 and S2 and NMR spectra. See DOI: https://doi.org/10.1039/d6ra00024j.

Acknowledgements

The authors are grateful to the Ministry of Science and Technology of Taiwan for financially supporting this research under the contracts NSTC 113-2811-M-077-001, NSTC 114-2811-M-077-001 and MOST 113-2113-M-077-001.

References

1 D. G. J. Larsson, Pollution from drug manufacturing: review and perspectives, *Philos. Trans. R. Soc., B*, 2014, **369**, 20130571; https://royalsocietypublishing.org/rstb/article/369/1656/20130571/58067/Pollution-from-drug-manufacturing-review-and.

2 M. M. Hossain, I. Jahan, M. A. Dar, M. J. Dhanavade, A. F. B. Mamtaz, S. J. Maxwell, S. Han and D. Zhu, A Review of potentially toxic elements in sediment, water, and aquatic species from the river ecosystems, *Toxics*, 2025, **13**, 26; https://www.mdpi.com/2305-6304/13/1/26.

3 T. E. Oladimeji, M. Oyedemi, M. E. Emetere, O. Agboola, J. B. Adeoye and O. A. Odunlami, Review on the impact of heavy metals from industrial wastewater effluent and removal technologies, *Heliyon*, 2024, **10**, e40370; https://www.sciencedirect.com/science/article/pii/S2405844024164018.

4 X. Li, X. Shen, W. Jiang, Y. Xi and S. Li, Comprehensive review of emerging contaminants: Detection technologies, environmental impact, and management strategies, *Ecotoxicol. Environ. Saf.*, 2024, **278**, 116420; https://www.sciencedirect.com/science/article/pii/S0147651324004962.

5 Y. Jurczynski, R. Passos and L. C. Campos, A Review of the most concerning chemical contaminants in drinking water for human health, *Sustainability*, 2024, **16**, 7107; https://www.mdpi.com/2071-1050/16/16/7107.

6 L. A. Thompson and W. S. Darwish, Environmental chemical contaminants in food: Review of a global problem, *J. Toxicol.*, 2019, **2019**, 2345283, DOI: 10.1155/2019/2345283.

7 F. Uddin, Environmental hazard in textile dyeing wastewater from local textile industry, *Cellulose*, 2021, **28**, 10715–10739, DOI: 10.1007/s10570-021-04228-4.

8 M. Shellaiah, K.-W. Sun, K. Anandan, A. Murugan, V. Venkatachalam, M. Bhushan, M. Sivakumar, E. Manikandan, K. Kaliaperumal and W.-T. Li, Luminescent pyrene-derivatives for Hg^{2+} and explosive detection, *Chemosensors*, 2025, **13**, 145; https://www.mdpi.com/2227-9040/13/4/145.

9 L. L. da Silva-Rêgo, L. A. de Almeida and J. Gasparotto, Toxicological effects of mining hazard elements, *Energy Geosci.*, 2022, **3**, 255–262; https://www.sciencedirect.com/science/article/pii/S266675922200021X.

10 S. Niu, Y. Xia, C. Yang and C. Liu, Impacts of the steel industry on sediment pollution by heavy metals in urban water system, *Environ. Pollut.*, 2023, **335**, 122364; https://www.sciencedirect.com/science/article/abs/pii/S0269749123013660.

11 V. Singh, G. Ahmed, S. Vedika, P. Kumar, S. K. Chaturvedi, S. N. Rai, E. Vamanu and A. Kumar, Toxic heavy metal ions contamination in water and their sustainable reduction by eco-friendly methods: isotherms, thermodynamics and kinetics study, *Sci. Rep.*, 2024, **14**, 7595; https://www.nature.com/articles/s41598-024-58061-3.

12 B. A. Sadee, S. M. S. Zebari, Y. Galali and M. F. Saleem, A review on arsenic contamination in drinking water: sources, health impacts, and remediation approaches, *RSC Adv.*, 2025, **15**, 2684–2703; https://pubs.rsc.org/en/content/articlelanding/2025/ra/d4ra08867k.

13 M. O. Wasonga, J. Maingi and O. Omwoyo, Effects of contamination of freshwater habitat with common heavy metals and anions on the prevalence of human adenoviruses and enteroviruses, *Front. Public Health*, 2021, **8**, 603217, DOI: 10.3389/fpubh.2020.603217/full.

14 T. B. Hendry-Hofer, P. C. Ng, A. E. Witeof, S. B. Mahon, M. Brenner, G. R. Boss and V. S. Bebarta, A Review on ingested cyanide: risks, clinical presentation, diagnostics, and treatment challenges, *J. Med. Toxicol.*, 2019, **15**, 128–133, DOI: 10.1007/s13181-018-0688-y.

15 J. I. Lachowicz, J. Alexander and J. O. Aaseth, Cyanide and cyanogenic compounds—toxicity, molecular targets, and therapeutic agents, *Biomolecules*, 2024, **14**, 1420; https://www.mdpi.com/2218-273X/14/11/1420.

16 X. Chen, Y. Ren, G. Qu, Z. Wang, Y. Yang and P. Ning, A review of environmental functional materials for cyanide removal by adsorption and catalysis, *Inorg. Chem. Commun.*, 2023, **157**, 111298; https://www.sciencedirect.com/science/article/abs/pii/S1387700323009103.

17 E. Jaszczak, Ż. Polkowska, S. Narkowicz and J. Namieśnik, Cyanides in the environment—analysis—problems and challenges, *Environ. Sci. Pollut. Res.*, 2017, **24**, 15929–15948, DOI: 10.1007/s11356-017-9081-7.

18 R. R. Dash, A. Gaur and C. Balomajumder, Cyanide in industrial wastewaters and its removal: A review on biotreatment, *J. Hazard. Mater.*, 2009, **163**, 1–11; https://www.sciencedirect.com/science/article/abs/pii/S0304389408009357.

19 K. Vaca-Escobar, D. Arregui-Almeida and P. Espinoza-Montero, Chemical, ecotoxicological characteristics, environmental fate, and treatment methods applied to cyanide-containing wastewater, *npj Clean Water*, 2024, **7**, 103; https://www.nature.com/articles/s41545-024-00392-9.

20 S. Sarkar, T. K. Ghosh, P. S. Dash, M. I. Shammas and S. Chakarborty, Generation & mitigation of cyanides: A steel industrial perspective, *Groundw. Sustain. Dev.*, 2025, **30**, 101463; https://www.sciencedirect.com/science/article/abs/pii/S2352801X25000608.

21 D. H. Jang, F. S. Shofer, S. L. Weiss and L. B. Becker, Impairment of mitochondrial respiration following ex vivo cyanide exposure in peripheral blood mononuclear cells, *Clin. Toxicol.*, 2016, **54**, 303–307, DOI: 10.3109/15563650.2016.1139712.

22 E. Alan-Albayrak and U. Simonsen, Cyanide beyond toxicity: A systematic review of its effects on vascular function, *Basic Clin. Pharmacol. Toxicol.*, 2025, **137**, e70124, DOI: 10.1111/bcpt.70124.

23 M. Ghosh, A. Biswas, A. Maji, S. Guha, G. Das, R. Naskar, S. Gharami and T. K. Mondal, A dual-phase coumarin-based ratiometric fluorescent probe for highly sensitive cyanide sensing and bioimaging applications, *Analyst*, 2025, **150**, 5072–5083; https://pubs.rsc.org/en/content/articlelanding/2025/an/d5an00816f.

24 S. Bhatt, G. Vyas and P. Paul, Rosmarinic acid-capped silver nanoparticles for colorimetric detection of CN^- and redox-modulated surface reaction-aided detection of Cr(VI) in water, *ACS Omega*, 2022, **7**, 1318–1328, DOI: 10.1021/acsomega.1c05946.

25 E. E. Kwaansa-Ansah, L. P. Amenorfe, E. K. Armah and F. Opoku, Human health risk assessment of cyanide levels in water and tuber crops from Kenyasi, a mining community in the Brong Ahafo Region of Ghana, *Int. J. Food Contam.*, 2017, **4**, 16, DOI: 10.1186/s40550-017-0061-y.

26 M. Shellaiah, E. Manikandan, K. W. Sun and V. Venkatachalam, Luminescent probes/conjugates derived from quantum dots, nanoparticles, and nanoclusters for cyanide (CN^-) detection, *Nano Express*, 2024, **5**, 042001, DOI: 10.1088/2632-959X/ad9297.

27 F. Luo, M. Guo, L. Zheng and Z. Cai, Efficient fluorescence-enhanced probe for cyanide ions based on a tetraphenylethene pyridine coordinated copper-iodide complex, *RSC Adv.*, 2023, **13**, 19738–19745; https://pubs.rsc.org/en/content/articlelanding/2023/ra/d3ra02868b.

28 X. Liu, H. Chen, X. Hu, J. Liu, X. Zhu, Y. Zhang and M. Liu, CN^- as a cofactor enhancing the laccase-like activity of copper porphyrin metal-organic frameworks facilitates the sensitive cyanide detection, *Sens. Actuators, B*, 2025, **442**, 138135; https://www.sciencedirect.com/science/article/abs/pii/S0925400525009116.

29 F. Wang, L. Wang, X. Chen and J. Yoon, Recent progress in the development of fluorometric and colorimetric chemosensors for detection of cyanide ions, *Chem. Soc. Rev.*, 2014, **43**, 4312–4324; https://pubs.rsc.org/en/content/articlelanding/2014/cs/c4cs00008k.

30 E. Kandemir, B. Aydıner, E. Şahin, Y. Sakalli, N. Seferoğlu and Z. Seferoğlu, Determination of cyanide in organic and aqueous environments by NASH reaction, *Dyes Pigm.*, 2025, **241**, 112898; https://www.sciencedirect.com/science/article/abs/pii/S0143720825002682.

31 S. Majeed, M. T. Waseem, H. M. Junaid, G. S. Khan, S. Nawazish, T. Mahmood, A. M. Khan and S. A. Shahzad, Aggregation induced emission based fluorenes as dual-channel fluorescent probes for rapid detection of cyanide: applications of smartphones and logic gates, *RSC Adv.*, 2022, **12**, 18897–18910; https://pubs.rsc.org/en/content/articlelanding/2022/ra/d2ra03119a.

32 J. Cao, M. Ouyang, C. Xu, H. Li, Z. Chen, L. Chen and D. Xu, Ultrafast sensitive colorimetric detection of cyanide based on dissolving AgI on Au-AgI heterodimeric nanoparticles via UV–vis spectroscopy and single nanoparticle imaging, *Sens. Actuators, B*, 2024, **410**, 135635; https://www.sciencedirect.com/science/article/abs/pii/S0925400524003642.

33 D. R. Goud, K. Sinha Roy, D. Pardasani, A. K. Purohit, V. K. Tak and D. K. Dubey, Gas chromatography-mass spectrometric identification of cyanide using a nucleophilic substitution based derivatization with S-phenyl benzenethiosulfonate, *Anal. Methods*, 2020, **12**,

5839–5845; https://pubs.rsc.org/en/content/articlelanding/2020/ay/d0ay01643h.

34 I. Kathuria, P. Sharma and S. Kumar, Colorimetric, fluorometric, and electrochemical sensing of cyanide ion in aqueous media using merocyanine-ferrocene conjugate, *J. Photochem. Photobiol., A*, 2023, **445**, 115081; https://www.sciencedirect.com/science/article/pii/S1010603023005464.

35 W. Shen, K. Wang, Q. Lu, W. Xie, S. Zhu, S. Yu, J. Chen and Q. Zhu, A chemiluminescence probe for the analysis of cyanide in biosamples and living cells, *J. Food Compos. Anal.*, 2025, **139**, 107077; https://www.sciencedirect.com/science/article/abs/pii/S0889157524011116.

36 S. D. Padghan, L.-C. Wang, W.-C. Lin, J.-W. Hu, W.-C. Liu and K.-Y. Chen, Rational design of an ICT-based chemodosimeter with aggregation-induced emission for colorimetric and ratiometric fluorescent detection of cyanide in a wide pH range, *ACS Omega*, 2021, **6**, 5287–5296, DOI: 10.1021/acsomega.0c05409.

37 M. K. Chahal and M. Sankar, Porphyrin chemodosimeters: synthesis, electrochemical redox properties and selective 'naked-eye' detection of cyanide ions, *RSC Adv.*, 2015, **5**, 99028–99036; https://pubs.rsc.org/en/content/articlelanding/2015/ra/c5ra19847j.

38 S. Lohar, K. Dhara, P. Roy, S. P. Sinha Babu and P. Chattopadhyay, Highly sensitive ratiometric chemosensor and biomarker for cyanide ions in the aqueous medium, *ACS Omega*, 2018, **3**, 10145–10153, DOI: 10.1021/acsomega.8b01035.

39 D. Jothi, S. Munusamy, S. Manickam, S. Enbanathan, S. Manojkumar and S. K. Iyer, Benzothiazole appended 2,2′-(1,4-phenylene) diacetonitrile for the colorimetric and fluorescence detection of cyanide ions, *RSC Adv.*, 2022, **12**, 30045–30050; https://pubs.rsc.org/en/content/articlelanding/2022/ra/d2ra03702e.

40 Y.-X. Hua, Y. Shao, Y.-W. Wang and Y. Peng, A series of fluorescent and colorimetric chemodosimeters for selective recognition of cyanide based on the FRET mechanism, *J. Org. Chem.*, 2017, **82**, 6259–6267, DOI: 10.1021/acs.joc.7b00850.

41 M. Shellaiah, B. Aazaad, M.-C. Lin, K.-W. Sun, A. Murugan, K. Anandan, M. Bhushan, M. Sivakumar and W.-T. Li, Commercial trans-β-nitrostyrene analogues for colorimetric cyanide (CN^-) detection via Michael addition-based chemodosimetric approach validated by comparative investigations, DFT, and strip method, *J. Photochem. Photobiol., A*, 2026, **472**, 116786; https://www.sciencedirect.com/science/article/abs/pii/S101060302500526X.

42 C. Yang and X. Luo, Tuning the electronic and optical properties of crystalline anthracene by doping and pressure for photovoltaic applications, *ACS Omega*, 2025, **10**, 4143–4153, DOI: 10.1021/acsomega.4c10572.

43 A. Szukalski, D. Zajac, N. Pardus, H. E. Karout, P. Krawczyk and B. Sahraoui, Unveiling all-optical switching phenomenon in anthracene derivatives: A comprehensive study on optical and nonlinear optical multifunctionality, *Adv. Opt. Mater.*, 2024, **12**, 2303156, DOI: 10.1002/adom.202303156.

44 M. Shellaiah, H.-C. Chen, K. Awasthi, B. Aazaad, K. W. Sun, N. Ohta and M.-C. Lin, An AIE active anthracene-based Schiff base probe for "turn-on" detection of Cu^{2+} ions: Demonstrations with nanostructural investigations, DFT, cellular imaging, and real water analysis, *J. Mol. Struct.*, 2024, **1301**, 137347; https://www.sciencedirect.com/science/article/abs/pii/S0022286023024353.

45 G. Punithakumari and S. Velmathi, Smart sensing of cyanide and iron(III) by anthracene-based probe through relay recognition approach, *J. Photochem. Photobiol., A*, 2019, **373**, 94–104; https://www.sciencedirect.com/science/article/abs/pii/S1010603018311250.

46 B. H. Shankar, D. T. Jayaram and D. Ramaiah, A reversible dual mode chemodosimeter for the detection of cyanide ions in natural sources, *Chem.–Asian J.*, 2014, **9**, 1636–1642, DOI: 10.1002/asia.201402008.

47 M. Viji, A. K. Nair, P. C. Nandajan and D. Ramaiah, Fluorescent chemodosimeter based on NHC complex for selective recognition of cyanide ions in aqueous medium, *RSC Adv.*, 2014, **4**, 47982–47986; https://pubs.rsc.org/en/content/articlelanding/2014/ra/c4ra09969a.

48 P. Yadav, A. Singh, G. Kumar, S. Singh and V. P. Singh, Anthracene appended AIEgen as a reversible fluorescence sensor for hazardous cyanide ion in environmental samples and fabrication of portable test kit for on-spot detection, *Spectrochim. Acta, Part A*, 2025, **329**, 125557; https://www.sciencedirect.com/science/article/abs/pii/S1386142524017232.

49 R. Iftikhar, I. Parveen, Ayesha, A. Mazhar, M. S. Iqbal, G. M. Kamal, F. Hafeez, A. L. Pang and M. Ahmadipour, Small organic molecules as fluorescent sensors for the detection of highly toxic heavy metal cations in portable water, *J. Environ. Chem. Eng.*, 2023, **11**, 109030; https://www.sciencedirect.com/science/article/abs/pii/S2213343722019030.

50 S. Li, Y. Xiao, C. Chen and L. Jia, Recent progress in organic small-molecule fluorescent probe detection of hydrogen peroxide, *ACS Omega*, 2022, **7**, 15267–15274, DOI: 10.1021/acsomega.2c00117.

51 X. Tian, Q. Wang, J. Jian, X. Yang and Z. Li, Small molecular organic fluorescent probes (SMOFPs) applied in food safety inspection from 2015 to 2025, *J. Agric. Food Chem.*, 2025, **73**, 19174–19203, DOI: 10.1021/acs.jafc.5c05522.

52 A. Irfan, S. A. Al-Hussain, T. Khalid, I. Nasim, M. Mojzych and M. E. A. Zaki, Recent advances in clinically approved nitrogenous heterocycle-based drugs and EGFR Tyrosine kinase inhibitors for precision oncology (2020–2024): a review, *J. Saudi Chem. Soc.*, 2025, **29**, 39, DOI: 10.1007/s44442-025-00040-y.

53 K. Nepali, H.-Y. Lee and J.-P. Liou, Nitro-Group-Containing Drugs, *J. Med. Chem.*, 2019, **62**, 2851–2893, DOI: 10.1021/acs.jmedchem.8b00147.

54 K. Anichina, N. Lumov, V. Bakov, D. Yancheva and N. Georgiev, Recent advances in the application of nitro(het)aromatic compounds for treating and/or

fluorescent imaging of tumor hypoxia, *Molecules*, 2024, **29**, 3475; https://www.mdpi.com/1420-3049/29/15/3475.

55 V. R. L. J. Bloemendal, M. A. C. H. Janssen, J. C. M. van Hest and F. P. J. T. Rutjes, Continuous one-flow multi-step synthesis of active pharmaceutical ingredients, *React. Chem. Eng.*, 2020, **5**, 1186–1197; https://pubs.rsc.org/en/content/articlelanding/2020/re/d0re00087f.

56 M. Bastrakov and A. Starosotnikov, Recent progress in the synthesis of drugs and bioactive molecules incorporating nitro(het)arene core, *Pharmaceuticals*, 2022, **15**, 705; https://www.mdpi.com/1424-8247/15/6/705.

57 B. Colin-Lozano, H. Torres-Gomez, S. Hidalgo-Figueroa, F. Chávez-Silva, S. Estrada-Soto, J. C. Almanza-Pérez and G. Navarrete-Vazquez, Synthesis, in vitro, in vivo and in silico antidiabetic bioassays of 4-Nitro(thio) phenoxyisobutyric acids acting as unexpected PPARγ modulators: An in combo study, *Pharmaceuticals*, 2022, **15**, 102; https://www.mdpi.com/1424-8247/15/1/102.

58 C. B. Meenakshy, K. S. Sandhya, R. Gouri, D. K. S. Lekshmi and A. Deepthi, Synthesis and anticancer evaluation of tryptanthrin appended spiro1-nitropyrrolizidine derivatives by the three-component reaction of tryptanthrin, L-proline and β-nitrostyrene, *J. Mol. Struct.*, 2025, **1334**, 141795; https://www.sciencedirect.com/science/article/abs/pii/S0022286025004818.

59 M. Faghih Akhlaghi, M. Daeihamed, S. A. Ayatollahi, F. Kobarfard and A. Ata, Design, synthesis and evaluation of substituted aryl-2-nitrovinyl derivatives as small molecules proteasome inhibitors, *Iran. J. Pharm. Res.*, 2018, **17**, 906–916; https://brieflands.com/journals/ijpr/articles/124795.

60 Z. Chen, Y. Zheng and J.-A. Ma, Use of a traceless activating and directing group for the construction of trifluoromethylpyrazoles: One-pot transformation of nitroolefins and trifluorodiazoethane, *Angew. Chem., Int. Ed.*, 2017, **56**, 4569–4574, DOI: 10.1002/anie.201700955.

61 S. Kadam, M. Shellaiah, W.-T. Li, P. Badani, K. Awasthi, N. Ohta and G. Chaturbhuj, A carbohydrazide-based Schiff base derivative for colorimetric and fluorometric detection of Cu^{2+}, Co^{2+}, and OH^- ions: Validation through DFT, test strips, cellular imaging, and real water analysis, *J. Photochem. Photobiol., A*, 2025, 11703; DOI: https://www.sciencedirect.com/science/article/abs/pii/S1010603025007531.

62 M. J. Frisch, *et al.*, *Gaussian 16, Revision C.01*, Gaussian, Inc., Wallingford CT, 2016; https://gaussian.com/citation/.

63 A. D. Becke, Density-functional exchange-energy approximation with correct asymptotic behavior, *Phys. Rev. A*, 1988, **38**, 3098–3100, DOI: 10.1103/PhysRevA.38.3098.

64 M. Shellaiah, K.-W. Sun, B. Aazaad, K. Awasthi, M.-C. Lin, N. Ohta and W.-T. Li, A perylene derivative for multi-hazard detection in environmental monitoring: Demonstration via DFT, cellular imaging, and real-time applications, *J. Hazard. Mater. Adv.*, 2025, **19**, 100863; https://www.sciencedirect.com/science/article/pii/S2772416625002748.

65 C. Huang, H. Mao, W. Wan, C. Ren, X. Ji, B. Yue, X. Zhang and Q. Wu, Extraction, content determination, component analysis, and pharmacological action of Hedysari flavonoids: a review of research progress, *Front. Pharmacol*, 2025, **16**, 1517832, DOI: 10.3389/fphar.2025.1517832/full.

66 M. Shellaiah, K. W. Sun, K. Anandan, M. Bhushan, A. Murugan and W.-T. Li, Biocompatible rhodamine functionalized nanodiamond for heavy metal ions detection: Demonstration by paper strips, cellular imaging, and real water investigations, *Diamond Relat. Mater.*, 2025, **158**, 112698; https://www.sciencedirect.com/science/article/abs/pii/S0925963525007551.

67 V. Vichai and K. Kirtikara, Sulfarhodamine B colorimetric assay for cytotoxicity screening, *Nat. Protoc.*, 2006, **1**, 1112–1116; https://www.nature.com/articles/nprot.2006.179.

68 J. Galvao, B. Davis, M. Tilley, E. Normando, M. R. Duchen and M. F. Cordeiro, Unexpected low-dose toxicity of the universal solvent DMSO, *FASEB J.*, 2014, **28**, 1317–1330, DOI: 10.1096/fj.13-235440.